Journal of Computational Physics 228 (2009) 8446–8466

Contents lists available at ScienceDirect

Journal of Computational Physics

journal homepage: www.elsevier.com/locate/jcp

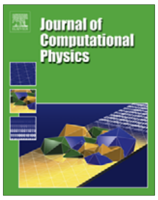

Numerical simulation of three-dimensional nonlinear water waves

Liwei Xu [a,b], Philippe Guyenne [a,*]

[a] Department of Mathematical Sciences, University of Delaware, 501 Ewing Hall, Newark, DE 19716-2553, USA
[b] College of Mathematics and Physics, Chongqing University, Chongqing 400044, China

ARTICLE INFO

Article history:
Received 5 November 2008
Received in revised form 21 May 2009
Accepted 19 August 2009
Available online 28 August 2009

Keywords:
Nonlinear water waves
Dirichlet–Neumann operator
Spectral methods
Three-dimensional domains

ABSTRACT

We present an accurate and efficient numerical model for the simulation of fully nonlinear (non-breaking), three-dimensional surface water waves on infinite or finite depth. As an extension of the work of Craig and Sulem [19], the numerical method is based on the reduction of the problem to a lower-dimensional Hamiltonian system involving surface quantities alone. This is accomplished by introducing the Dirichlet–Neumann operator which is described in terms of its Taylor series expansion in homogeneous powers of the surface elevation. Each term in this Taylor series can be computed efficiently using the fast Fourier transform. An important contribution of this paper is the development and implementation of a symplectic implicit scheme for the time integration of the Hamiltonian equations of motion, as well as detailed numerical tests on the convergence of the Dirichlet–Neumann operator. The performance of the model is illustrated by simulating the long-time evolution of two-dimensional steadily progressing waves, as well as the development of three-dimensional (short-crested) nonlinear waves, both in deep and shallow water.

1. Introduction

The water wave problem has been a subject of scientific investigation for many years. It entails considerable mathematical and computational challenges due to the nonlinear character of the governing equations. It is also of great practical importance in applications to coastal engineering and oceanography; e.g. to improve the design of coastal and offshore structures, and to better understand ocean dynamics and air–sea interactions.

The water wave problem usually refers to the problem of solving the Euler equations for potential flow with a free surface, under the influence of gravity and surface tension. Because of the complexity of these equations, simplified models have been extensively used as an alternative. Two asymptotic scaling regimes are of particular interest: the long-wave regime and the modulational regime. In the long-wave regime, water waves have been typically modeled using Boussinesq and shallow water-type equations [5,6]. Over the years, much effort has been devoted to improve the dispersive and nonlinear properties of these equations and, as a result, the current generation of Boussinesq models has reached a high degree of sophistication, being applicable to highly nonlinear waves, shorter wavelengths and deeper water [29,27]. Other related long-wave models can be found in [44,45].

In the modulational regime, the nonlinear Schrödinger (NLS) equation and its higher-order versions have been the preferred tool for prediction [61]. These models have been extensively used to study the evolution of quasi-monochromatic waves and their instabilities due to resonant interactions (e.g. the Benjamin–Feir instability). Extensions of the NLS equation also include the Zakharov equation which has been applied to the long-time description of the spectrum of weakly nonlinear,

---

[*] Corresponding author. Tel.: +1 302 831 8664; fax: +1 302 831 4511.
E-mail addresses: xul@math.udel.edu (L. Xu), guyenne@math.udel.edu (P. Guyenne).

0021-9991/$ - see front matter © 2009 Elsevier Inc. All rights reserved.
doi:10.1016/j.jcp.2009.08.015

dispersive waves. In particular, recent studies have used the NLS and Zakharov equations to investigate the statistics of rogue waves and their occurrence as a result of four-wave interactions [38,54,52,28].

In recent years, progress in both mathematical techniques and computer power has led to a rapid development of numerical models solving directly the Euler equations. These models can be divided into two main categories: boundary integral methods [2,4,10,30,60,36,24,22,31] and spectral methods. In particular, spectral methods based on perturbation expansions have been known to be very efficient [20,59,19,46,3]. These two methods reduce the water wave problem from one posed inside the entire fluid domain to one posed on the boundary alone, thus reducing the dimension of the formulation. This reduction can be accomplished by using integral equations over the boundary of the domain (boundary integral methods), or by introducing boundary quantities which can be expanded as Taylor series about a reference geometry of the domain (as in spectral methods).

Moreover, there has been a growing interest in the development of three-dimensional models which, combined with full dispersion and full nonlinearity, are capable of dealing with a wide range of water-wave problems. Real sea states are both broad-banded in frequency and direction. It is this broad-bandedness that poses some of the most significant difficulties in terms of numerical simulation; the importance of directionality and the benefits of efficient wave modeling being clearly demonstrated by Bateman et al. [3] who compared numerical simulations with laboratory observations of Johannessen and Swan [39]. This is the motivation for the present study which aims at contributing further in this direction of inquiry.

In this paper, we present a new numerical model for fully nonlinear, three-dimensional water waves which extends that of Craig and Sulem [19] originally given in the two-dimensional setting. The model is based upon Zakharov's Hamiltonian formulation [61] in which the problem is reduced to a lower-dimensional computation involving surface variables alone. This is made possible by introducing the Dirichlet–Neumann operator (DNO) which, in light of its analyticity properties, is expressed in terms of its Taylor series expansion in homogeneous powers of the surface elevation. Each term in this Taylor series can be obtained from a recursion formula and can be efficiently computed by a pseudospectral method using the fast Fourier transform. Here we will only pay attention to surface water waves propagating in deep water or on uniform depth, although this is not a restriction of the model which can be extended to include a variable bottom topography [15,32]. The latter references consider smooth topographies of small amplitude. Two-dimensional cases of nonsmooth, large-amplitude topographies were considered in [1] through the DNO approach.

Our new contributions are: (i) the development and implementation of a symplectic, implicit, fourth-order Runge–Kutta scheme for the time integration of the Hamiltonian equations of motion, (ii) extensive numerical tests on the convergence of the DNO and on the accuracy of the time integration method, including an examination of the effects of de-aliasing and filtering, and (iii) applications to a number of three-dimensional, nonlinear wave solutions ranging from crescent waves in deep water to hexagonal waves in shallow water. To our knowledge, computations of such waves by a surface-perturbation, spectral method solving the fully nonlinear time-dependent Euler equations are reported for the first time here.

The present work is most closely related to those of Schanz [53], Nicholls [46] (see also [17]) and Bateman et al. [3], in the sense that the full Euler equations for three-dimensional irrotational water waves are solved using an expansion of the DNO along with a Fourier spectral discretization. However, Nicholls [46] only focused on computing steadily progressing wave solutions using a numerical continuation method, and thus did not solve explicitly the time evolution problem. Schanz [53] performed time-dependent simulations using a three-dimensional extension of Craig and Sulem's model [19]. However, he did not employ a symplectic integrator and did not take advantage of the self-adjoint property of the DNO (see Section 3.1). In particular, he did not simulate any three-dimensional wave patterns such as crescent, rectangular or hexagonal waves. Bateman et al. [3] used a definition of the DNO different from ours, and therefore the corresponding recursion formula, the equations of motion and their implementation also differ from ours. More specifically, Bateman et al. [3] defined the DNO (their G-operator) related to the vertical fluid velocity at the free surface (similarly to [20,59]), while we define the DNO related to the normal fluid velocity at the free surface (similarly to [19,46]). This difference in definition has consequences on the properties and implementation of the DNO; further discussion will be provided in Section 3.1.

The remainder of the paper is organized as follows. In Section 2, we present the mathematical formulation of the problem, including the Hamiltonian formulation of the equations of motion and the Taylor series expansion of the DNO. In Section 3, we describe the numerical methods for spatial and temporal discretization in the model, including the symplectic time integration method and the procedures for de-aliasing and filtering. Finally, Section 4 presents numerical tests on the convergence of the DNO and on the accuracy of the time integration method, as well as applications to three-dimensional nonlinear waves. Concluding remarks are given in Section 5.

2. Mathematical formulation

2.1. Governing equations and Hamiltonian formulation

We consider the evolution of a free surface on top of a three-dimensional fluid under the influence of gravity. Let $x = (x_1, x_2)$ denote the horizontal plane, y the vertical direction and t time. The impermeable bottom is fixed at constant depth $y = -h$. The fluid is assumed to be incompressible, inviscid and the flow is irrotational, so that the fluid velocity is given by $u = \nabla\varphi$ and the velocity potential $\varphi(x, y, t)$ satisfies the Laplace equation

$$\nabla^2\varphi = 0 \tag{1}$$

in the fluid region bounded below by the bottom at $\{y = -h\}$ and above by the free surface defined by the graph $\{y = \eta(x,t), x \in \mathbb{R}^2, t \geqslant 0\}$. The boundary conditions are

$$\partial_y \varphi = 0 \quad \text{on } y = -h, \tag{2}$$

$$\partial_t \eta + \nabla_x \eta \cdot \nabla_x \varphi - \partial_y \varphi = 0 \quad \text{on } y = \eta, \tag{3}$$

$$\partial_t \varphi + \frac{1}{2}|\nabla \varphi|^2 + g\eta = 0 \quad \text{on } y = \eta, \tag{4}$$

where $\nabla_x = (\partial_{x_1}, \partial_{x_2})^\top$ and g denotes the acceleration due to gravity. Surface tension effects are neglected here but could easily be incorporated [16].

Following Craig and Sulem [19], we can reduce the dimensionality of the classical potential flow formulation (1)–(4) of the water wave problem by considering surface quantities as unknowns. This can be achieved by introducing the Dirichlet–Neumann operator (DNO) which takes Dirichlet data $\xi(x,t) = \varphi(x, \eta(x,t), t)$ at the free surface, solves the Laplace equation (1) for φ, and returns the corresponding Neumann data (i.e. the normal fluid velocity at the free surface). Here the DNO is defined by

$$G(\eta)\xi = (-\nabla_x \eta, 1)^\top \cdot \nabla \varphi|_{y=\eta}. \tag{5}$$

Expressing the velocity potential and its derivatives on the free surface in terms of ξ and $G(\eta)\xi$, and knowing that (1) and (2) are already satisfied through (5), then we can rewrite (3) and (4) as (see [19,46])

$$\partial_t \eta = G(\eta)\xi, \tag{6}$$

$$\partial_t \xi = -g\eta - \frac{1}{2(1+|\nabla_x \eta|^2)}\Big[|\nabla_x \xi|^2 - (G(\eta)\xi)^2 - 2(G(\eta)\xi)\nabla_x \xi \cdot \nabla_x \eta + |\nabla_x \xi|^2 |\nabla_x \eta|^2 - (\nabla_x \xi \cdot \nabla_x \eta)^2\Big]. \tag{7}$$

These are Hamilton's equations in Zakharov's formulation [61] of the water wave problem in terms of the canonically conjugate variables η and ξ, which can be expressed in canonical form

$$\partial_t \begin{pmatrix} \eta \\ \xi \end{pmatrix} = \begin{pmatrix} 0 & 1 \\ -1 & 0 \end{pmatrix} \begin{pmatrix} \delta_\eta H \\ \delta_\xi H \end{pmatrix}, \tag{8}$$

with Hamiltonian

$$H = \frac{1}{2}\int_{\mathbb{R}^2} [\xi G(\eta)\xi + g\eta^2] dx. \tag{9}$$

Eq. (9) represents the total energy of the system and, together with the total mass (or volume) due to the surface disturbance,

$$V = \int_{\mathbb{R}^2} \eta dx \tag{10}$$

is an invariant of motion in the problem. As will be shown in Section 4, mass and energy conservation can be used to check the global accuracy of our numerical model.

2.2. Dirichlet–Neumann operator

Coifman and Meyer [11] showed that, if $\eta \in \mathrm{Lip}(\mathrm{R})$, then G is an analytic function of η, from which it follows that G can be written in terms of a convergent Taylor series

$$G(\eta) = \sum_{j=0}^{\infty} G_j(\eta), \tag{11}$$

where the Taylor polynomials G_j are homogeneous of degree j in η. Craig et al. [18] extended this result for periodic $\eta \in C^1(\mathbb{R}^2)$, and Craig and Nicholls [16] generalized it for $\eta \in C^1(\mathbb{R}^n), n \geqslant 2$. Further analyticity results can be found in [48].

Craig and Sulem [19] showed that explicit expressions for the G_j's can be obtained using a recursion formula, which was generalized to three dimensions by Craig et al. [18], Nicholls [46], and Craig and Nicholls [17]:

For $j = 2r > 0$,

$$\begin{aligned} G_{2r}(\eta) = {} & \frac{1}{(2r)!} G_0 \left(|D_x|^2\right)^{r-1} D_x \cdot \eta^{2r} D_x - \sum_{s=0}^{r-1} \frac{1}{(2(r-s))!} \left(|D_x|^2\right)^{r-s} \eta^{2(r-s)} G_{2s}(\eta) \\ & - \sum_{s=0}^{r-1} \frac{1}{(2(r-s)-1)!} G_0 \left(|D_x|^2\right)^{r-s-1} \eta^{2(r-s)-1} G_{2s+1}(\eta) \end{aligned} \tag{12}$$

and, for $j = 2r - 1 > 0$,

$$G_{2r-1}(\eta) = \frac{1}{(2r-1)!}\left(|D_x|^2\right)^{r-1} D_x \cdot \eta^{2r-1} D_x - \sum_{s=0}^{r-1} \frac{1}{(2(r-s)-1)!} G_0 \left(|D_x|^2\right)^{r-s-1} \eta^{2(r-s)-1} G_{2s}(\eta)$$
$$- \sum_{s=0}^{r-2} \frac{1}{(2(r-s-1))!}\left(|D_x|^2\right)^{r-s-1} \eta^{2(r-s-1)} G_{2s+1}(\eta), \qquad (13)$$

where $D_x = -i\nabla_x$ and $G_0 = G(0) = |D_x| \tanh(h|D_x|)$ represent Fourier multiplier operators. In the infinite-depth case $(h = +\infty)$, G_0 reduces to $|D_x|$.

This formulation of the water wave problem is convenient for the numerical simulation of three-dimensional nonlinear waves as presented in this paper, as well as in a number of other settings. These include numerical and asymptotic studies of surface waves over a rough bottom [15,32,7], and waves at the interface between immiscible fluids [14]. It is also understood that overturning waves (i.e. a multi-valued free surface) cannot be described with this formulation.

3. Numerical methods

In this section, we describe the numerical methods for spatial and temporal discretizations of the model. We also discuss the implementation of zero-padding and filtering techniques to remove aliasing errors and numerical instabilities.

3.1. Spatial discretization

We assume periodic boundary conditions in x and use a pseudospectral method [8] for spatial discretization of the DNO as well as the equations of motion (6), (7). This is a natural choice for the computation of G since each term in its Taylor series expansion (11) consists of concatenations of Fourier multipliers with powers of η. More specifically, both functions η and ξ are expanded in truncated Fourier series

$$\begin{pmatrix} \eta \\ \xi \end{pmatrix} = \sum_k \begin{pmatrix} \hat{\eta}_k \\ \hat{\xi}_k \end{pmatrix} e^{ik\cdot x}, \qquad (14)$$

where $k = (k_1, k_2)$ denotes the wavenumbers. Applications of Fourier multipliers are performed in Fourier space, while nonlinear products are calculated in physical space on a grid of $N_1 \times N_2$ points, equally spaced in each direction. For example, if we wish to apply the zeroth-order operator G_0 to a function ξ in physical space, we transform ξ to Fourier space, apply the diagonal operator $|k| \tanh(h|k|)$ to the Fourier coefficients of ξ, and then transform back to physical space. All operations are performed using the FFTW library [23].

In computations, the Taylor series of G is also truncated by only retaining a finite number of terms,

$$G(\eta) \approx G^M(\eta) = \sum_{j=0}^{M} G_j(\eta), \qquad (15)$$

where the order of truncation M is chosen according to the physical problem under consideration. As will be shown below in our numerical tests and applications, it is sufficient to select a small number of terms $(M < 10)$ for satisfactory results, even in cases of fairly large-amplitude and steep waves.

We note that formulas (12) and (13) are slightly different from those given in [19,46] regarding the order of application of the various operators. As pointed out by Craig and Nicholls [17], the DNO (5) is self-adjoint and therefore the adjoint formulas (12) and (13) are equivalent to the original ones. This property however has important consequences on the implementation of the DNO and on the computational efficiency of the model. In particular, the adjoint recursion formulas allow us to store and reuse the G_j's as vector operations on ξ, instead of having to recompute them at each order when applied to concatenations of Fourier multipliers and powers of η. This results in faster calculations, and the computational effort can be estimated to be $O(M^2 N \log N)$ operations per time step, where N is the total number of grid points. In contrast, the G-operator related to the vertical fluid velocity at the free surface, as defined by Bateman et al. [3], does not possess the self-adjoint property (although these authors were able to devise a fast algorithm based on the elimination of repeated calculations in their recursion formulas).

3.2. Time integration

Time integration of system (6) and (7) is performed in Fourier space, so the linear terms can be solved exactly by integrating factor technique. To this aim, we first separate the linear and nonlinear parts in (6) and (7). Defining $u = (\eta, \xi)^\top$, the equations of motion can be written in the form

$$\partial_t u = \mathcal{L}(u) + \mathcal{N}(u), \qquad (16)$$

where the linear contribution $\mathcal{L}(u)$ is defined by

$$\mathcal{L}(u) = \mathcal{A}u = \begin{pmatrix} 0 & G_0 \\ -g & 0 \end{pmatrix}\begin{pmatrix} \eta \\ \xi \end{pmatrix} \qquad (17)$$

and the nonlinear contribution $\mathcal{N}(u)$ by

$$\mathcal{N}(u) = \begin{pmatrix} (G(\eta) - G_0)\xi \\ -\frac{1}{2(1+|\nabla_x\eta|^2)}\left[|\nabla_x\xi|^2 - (G(\eta)\xi)^2 - 2(G(\eta)\xi)\nabla_x\xi\cdot\nabla_x\eta + |\nabla_x\xi|^2|\nabla_x\eta|^2 - (\nabla_x\xi\cdot\nabla_x\eta)^2\right] \end{pmatrix}.$$

Then, taking the Fourier transform and making the change of variables

$$\hat{u}_k(t) = \phi(t)\hat{v}_k(t), \tag{18}$$

where

$$\phi(t) = \begin{pmatrix} \cos(t\sqrt{gG_0}) & \sqrt{\frac{G_0}{g}}\sin(t\sqrt{gG_0}) \\ -\sqrt{\frac{g}{G_0}}\sin(t\sqrt{gG_0}) & \cos(t\sqrt{gG_0}) \end{pmatrix} \tag{19}$$

is the fundamental matrix of the linear system

$$\partial_t\hat{u}_k = \mathcal{A}\hat{u}_k, \tag{20}$$

we obtain the following nonlinear system for $\hat{v}_k$

$$\partial_t\hat{v}_k = \phi^{-1}\mathcal{N}(\phi\hat{v}_k) = \widetilde{\mathcal{N}}(\hat{v}_k). \tag{21}$$

Eq. (21) is solved numerically in time using a symplectic scheme, motivated by the fact that (6), (7) form a Hamiltonian system and the change of variables (18) is a canonical transformation. The latter property can be verified by showing that the symplectic structure J_2 associated with the new variable $\hat{v}_k$ is identical to the symplectic structure J associated with $\hat{u}_k$, where

$$J = \begin{pmatrix} 0 & 1 \\ -1 & 0 \end{pmatrix} \tag{22}$$

according to (8). Indeed, using the Hamiltonian transformation theory developed in [14], it is a straightforward calculation to show that

$$J_2 = \phi^{-1}J(\phi^{-1})^\top = J \tag{23}$$

given the fact that $\phi^{-1}(t) = \phi(-t)$.

Symplectic integrators have been known to capture the properties of Hamiltonian systems more correctly than standard integrators would do (e.g. for the long-time dynamics) [41]. Besides symplecticity, it is also desirable that the numerical scheme be of high order of accuracy since we are dealing with a nonlinear time-evolution problem. Explicit high-order symplectic methods (splitting methods) can be used when the Hamiltonian is separable in the two canonical variables, or when it is separable in linear and nonlinear parts which are exactly solvable [43]. However this is not the case here due to the coupling between η and ξ through the DNO, and the nonlocal nonlinear character of this operator. Therefore we have opted for an implicit symplectic scheme: the fourth-order (2-stage) Gauss–Legendre Runge–Kutta method [41]. Although we need to solve a large nonlinear system at each time step, we have found that this scheme gives accurate results at a reasonable cost.

Applied to (21), it gives

$$\begin{aligned} \hat{v}_k^{n+1} &= \hat{v}_k^n + \Delta t\left[b_1\widetilde{\mathcal{N}}\left(\hat{v}_k^{(1)}\right) + b_2\widetilde{\mathcal{N}}\left(\hat{v}_k^{(2)}\right)\right], \\ \hat{v}_k^{(1)} &= \hat{v}_k^n + \Delta t\left[a_{11}\widetilde{\mathcal{N}}\left(\hat{v}_k^{(1)}\right) + a_{12}\widetilde{\mathcal{N}}\left(\hat{v}_k^{(2)}\right)\right], \\ \hat{v}_k^{(2)} &= \hat{v}_k^n + \Delta t\left[a_{21}\widetilde{\mathcal{N}}\left(\hat{v}_k^{(1)}\right) + a_{22}\widetilde{\mathcal{N}}\left(\hat{v}_k^{(2)}\right)\right] \end{aligned} \tag{24}$$

for the solution at time $t_{n+1} = t_n + \Delta t$, where Δt denotes the (constant) time step and

$$\begin{aligned} &a_{11} = a_{22} = \frac{1}{4}, \quad a_{12} = \frac{1}{4} + \frac{\sqrt{3}}{6}, \quad a_{21} = \frac{1}{4} - \frac{\sqrt{3}}{6}, \\ &b_1 = b_2 = \frac{1}{2}, \\ &c_1 = \frac{1}{2} + \frac{\sqrt{3}}{6}, \quad c_2 = \frac{1}{2} - \frac{\sqrt{3}}{6}. \end{aligned}$$

We then change back to $\hat{u}_k$ by inverting (18) and rewrite (24) as

$$\hat{u}_k^{n+1} = \phi(\Delta t)\hat{u}_k^n + \Delta t\phi(\Delta t)\left[b_1\phi^{-1}(c_1\Delta t)\mathcal{N}\left(\phi(c_1\Delta t)\hat{u}_k^{(1)}\right) + b_2\phi^{-1}(c_2\Delta t)\mathcal{N}\left(\phi(c_2\Delta t)\hat{u}_k^{(2)}\right)\right], \tag{25}$$

$$\hat{u}_k^{(1)} = \hat{u}_k^n + \Delta t a_{11}\phi^{-1}(c_1\Delta t)\mathcal{N}\left(\phi(c_1\Delta t)\hat{u}_k^{(1)}\right) + \Delta t a_{12}\phi^{-1}(c_2\Delta t)\mathcal{N}\left(\phi(c_2\Delta t)\hat{u}_k^{(2)}\right), \tag{26}$$

$$\hat{u}_k^{(2)} = \hat{u}_k^n + \Delta t a_{21}\phi^{-1}(c_1\Delta t)\mathcal{N}\left(\phi(c_1\Delta t)\hat{u}_k^{(1)}\right) + \Delta t a_{22}\phi^{-1}(c_2\Delta t)\mathcal{N}\left(\phi(c_2\Delta t)\hat{u}_k^{(2)}\right). \tag{27}$$

At each time step, the nonlinear system (26) and (27) for $\hat{u}_k^{(1)}$ and $\hat{u}_k^{(2)}$ is solved by fixed-point iteration, with their initial guesses given by the solution $\hat{u}_k^n$ at time t_n. These intermediate solutions are then used in (25) to find $\hat{u}_k^{n+1}$. For all the applications shown in this paper, we have typically found that the nonlinear system can be solved in 2–4 iterations within a relative error of 10^{-6}—10^{-8}. We have typically used $\Delta t = 0.01$ which, in the case where the initial condition is close to a Stokes or plane wave, is chosen so that it is hundreds times smaller than the wave period. Given the fourth-order accuracy of the time integration scheme, this value of Δt is quite reasonable. We have also observed that using a smaller time step does not generally yield much better results partly because, to achieve the same simulation time, more computations of the DNO are required, thus introducing more numerical errors (see Section 4.1).

For a run involving a Stokes wave of amplitude $a = 0.15$, with $M = 4$ and $N_1 \times N_2 = 128 \times 128$, the CPU time is about 2 s per time step on a PC workstation (3 GHz processor).

3.3. De-aliasing and filtering

Two major sources of numerical error in the present model are aliasing and spurious growth of high-wavenumber errors. Aliasing is inherent to the pseudospectral method when applied to nonlinear equations [8]. Possible causes for high-wavenumber errors are the ill-conditioning of the expansion method for the DNO [48] which generates high-order derivative terms and relies heavily on cancellations, as well as nonlinear interactions. These lead to amplification of round-off and truncation errors, most severely in the highest Fourier modes of the solution, which can destabilize the computations. The larger the wave amplitude, the more significant these effects (see Section 4.1).

Aliasing occurs when evaluating the DNO and the equations of motion. The jth term $G_j(\eta)\xi$ in the DNO involves nonlinearities of order $j+1$ so aliasing errors may accumulate quickly for large j. Complete de-aliasing of the DNO truncated at order M requires applying an ideal low-pass filter to both $\hat{\eta}_k$ and $\hat{\xi}_k$ of the form

$$\gamma_k = \begin{cases} 1 & \text{if} \quad |k| \leqslant \nu |k_{\max}|, \\ 0 & \text{if} \quad |k| > \nu |k_{\max}|, \end{cases} \tag{28}$$

where $\nu = 1/(M+1)$. This is equivalent to increasing the spectral resolution of η and ξ by a factor of $M+1$, and setting the values of the extra modes to zero (zero-padding technique). This de-aliasing procedure was used in [46,13]. However, in the present three-dimensional time-dependent situation, it requires substantial memory storage which eventually affects the computational time. Keep in mind that multiple evaluations of G are performed in solving the nonlinear system (26) and (27) at each time step. Instead, we have applied zero padding by extending the spectra by a factor of $M/2+1$, which represents a reasonable compromise between partial de-aliasing and saving in memory storage (and thus in computational time). In the same way and for the same practical reasons, the computation of nonlinear terms in the equations of motion (6) and (7) is partially de-aliased by extending the spectra by a factor of 2.

In order to control the growth of high-wavenumber errors, we have tested and used two types of low-pass filters: an ideal filter of the form (28) with typically $\nu = 0.9$ and the exponential filter

$$\gamma_k = e^{-\alpha \left| \frac{k}{k_{\max}} \right|^m} \tag{29}$$

proposed by Hou and Li [35], with $\alpha = m = 36$. These filters are applied to both $\hat{\eta}_k$ and $\hat{\xi}_k$ at every time step. An advantage of (29) is that it falls off rapidly but smoothly at high wavenumbers, thus allowing for a better small-scale resolution than with the ideal filter. We have observed that the simulations of Stokes waves can be run a bit longer (i.e. for a few more time steps)

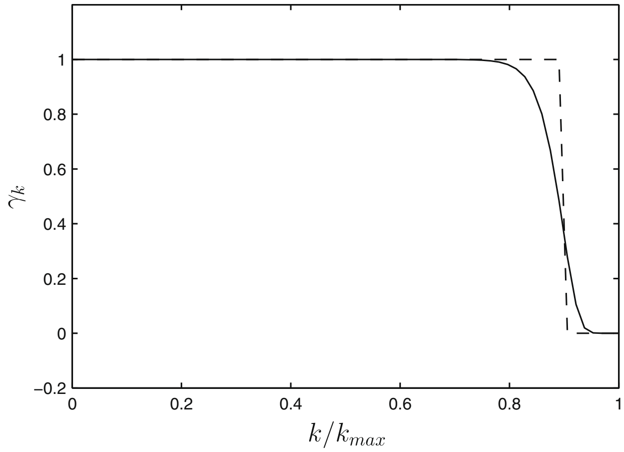

Fig. 1. Two-dimensional profiles of the ideal filter (28) with $\nu = 0.9$, in dashed line, and Hou and Li's [35] exponential filter (29), in solid line.

using the exponential filter, while the simulations of solitary waves can be run a bit longer using the ideal filter but, overall, both filters give similar results in terms of accuracy and run time. Profiles of these two filters are shown in Fig. 1. For a fixed Δt, we usually need to use filtering for large-amplitude/steep waves, large M and/or large N to run computations over a sufficiently long time.

4. Numerical tests

In this section, we present several tests to assess the performance of our numerical model and its ability to handle different types of solution. First, we examine the convergence of the DNO as a function of various numerical and physical parameters. We then test our symplectic time integrator by simulating the long-time evolution of two types of steadily progressing waves, Stokes waves in deep water and solitary waves in shallow water, as well as the recurrence phenomenon associated with the Benjamin–Feir instability of a Stokes wave. Finally, we apply our model to the computation of three-dimensional short-crested waves both in deep and shallow water, including crescent, rectangular and hexagonal waves.

We non-dimensionalize the variables in the following way: lengths are multiplied by k_0 and times by $\sqrt{gk_0}$ in the deep-water regime (where k_0 is a characteristic wavenumber), while lengths are divided by h and times by $\sqrt{h/g}$ in the shallow-water regime, so that g is always equal to 1.

4.1. Truncation order

The DNO has been shown to be analytic in η under certain regularity conditions on the free surface [11,18,16,48], which implies that it can be written in terms of a convergent Taylor series and the convergence is exponential with the order of truncation. We have checked this property in the present model by comparing the numerical approximation (15) of G with an exact expression, using the harmonic solution

$$\varphi(x,y) = \frac{ag}{\omega}\frac{\cosh(|k|(y+h))}{\cosh(|k|h)}\sin(k\cdot x), \tag{30}$$

with

$$\eta(x) = a\cos(k\cdot x). \tag{31}$$

Here a is the wave amplitude and $\omega = \sqrt{g|k|\tanh(|k|h)}$ is the linear dispersion relation. An exact expression of G can be obtained by inserting (30) and (31) into (5), yielding

$$G^E(\eta)\xi = \partial_y\varphi - \nabla_x\eta\cdot\nabla_x\varphi|_{y=\eta}, = \frac{ag}{\omega\cosh(|k|h)}[|k|\sinh(|k|(\eta+h))\sin(k\cdot x) - \nabla_x\eta\cdot k\cosh(|k|(\eta+h))\cos(k\cdot x)]. \tag{32}$$

Fig. 2(a) and (b) shows the L^2 error between G^M and G^E as a function of M, for different values of a and N_1 (with $N_2 = N_1$). For these tests, we have specified a domain of size $[0,2\pi]\times[0,2\pi]$ with $h = 1$ and $k = (k_1,k_2) = (1,1)$.

A first observation is that the exponential convergence with M is reproduced well in all the cases considered. As expected, the larger the wave amplitude, the smaller the rate of convergence (Fig. 2a). For small amplitudes, the convergence is so fast that machine precision is quickly reached, explaining the plateau starting at e.g. $M = 6$ for $a = 0.01$. We also see that, when a is large, there is an optimal value of M beyond which numerical errors quickly accumulate and convergence deteriorates. This phenomenon is related to the ill-conditioning of the expansion method for the DNO [3,48,49]. From Fig. 2(a), this optimal value is $M = 11$. The same feature can be observed in Fig. 2(b) which shows the convergence for a fixed amplitude but different spatial resolutions. The convergence rate is identical for the five cases considered but the optimal value of M varies depending on the resolution. The finer the resolution, the smaller the optimal value. We have also examined the influence of de-aliasing on the convergence of the DNO, which is illustrated in Fig. 2(c) for a typical case ($a = 0.2$). It can be seen that the loss of convergence in the de-aliased computation occurs at a value of M larger than in the aliased one. This indicates that the de-aliasing technique is effective at reducing numerical errors in the evaluation of the DNO. Needless to say that it is important to reduce numerical errors as much as possible at this stage since they may accumulate quickly due to the nonlinearity in the equations of motion and to the integration in time.

We note that Bateman et al. [3] and Nicholls and Reitich [49] obtained similar convergence results for varying wave amplitudes and spatial resolutions. However, Bateman et al. [3] did not examine the convergence of their DNO through a direct calculation. Instead, they analyzed the error on surface velocities by comparing their numerical solution with a fifth-order approximation of the Stokes wave. Here we test the convergence of the DNO directly by comparing its Taylor series expansion with an exact analytical expression.

From the previous discussion, the larger M, the more accurate the computation of the DNO. However, convergence may quickly deteriorate if M is too large, and this phenomenon is aggravated in the case of large-amplitude or highly deformed waves. Keep also in mind that the larger M, the more computation this requires. Therefore, for most of our applications, we have used $M = 4$ which represents a good compromise between accuracy and speed (see Fig. 2). We have systematically checked that using a larger value of M(<10) gives similar results.

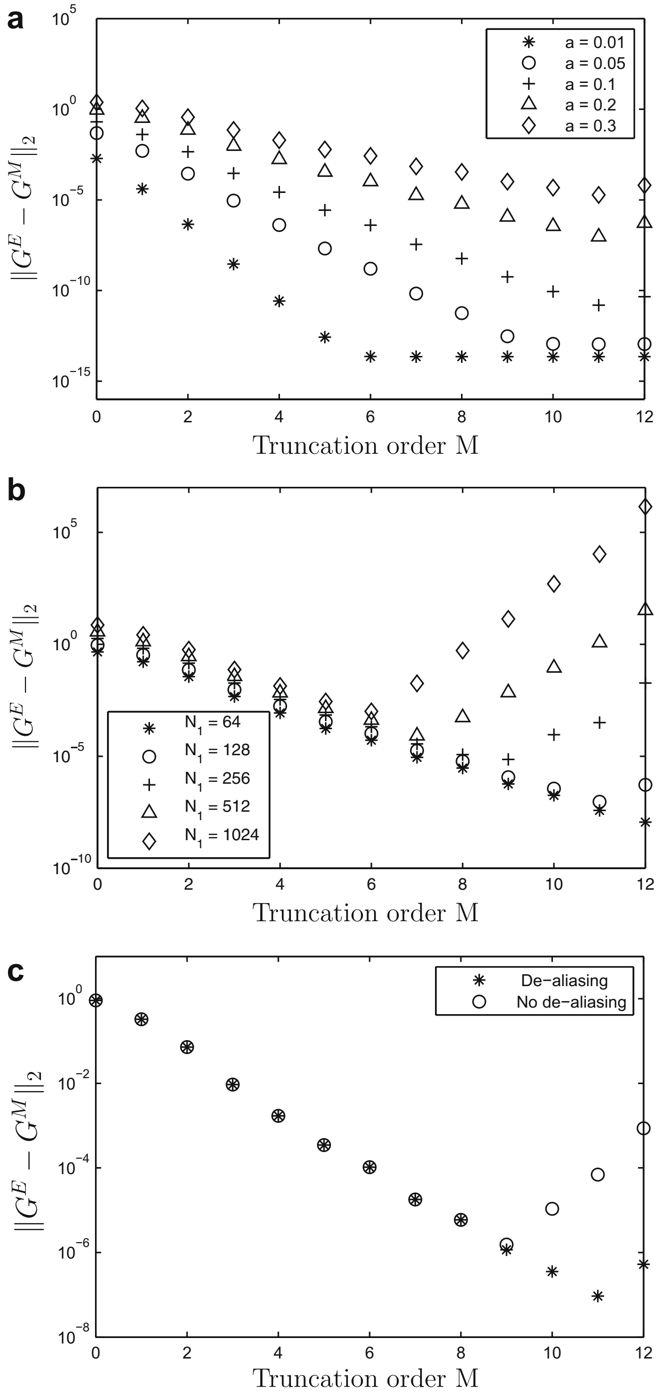

Fig. 2. L^2 errors on the Dirichlet–Neumann operator as functions of truncation order M for (a) varying amplitudes a $(N_1 = N_2 = 128)$, (b) varying resolutions N_1 $(a = 0.2,\ N_2 = N_1)$, and (c) with/without de-aliasing $(a = 0.2,\ N_1 = N_2 = 128)$.

4.2. Long-time integration

The conservative properties of our symplectic time integrator have been tested by simulating the long-time evolution of two types of steadily progressing waves, Stokes waves in deep water and solitary waves in shallow water, as well as the recurrence phenomenon associated with the Benjamin–Feir instability of a Stokes wave. These three test cases are two-dimensional in space. We will also discuss the use of filtering to stabilize computations in the case of large-amplitude solutions.

4.2.1. Progressive Stokes waves

We first consider the propagation of a progressive Stokes wave of steepness $k_1 a = 0.15$ in deep water ($h = +\infty$). We choose $k_1 = 1$ so that the wave amplitude is $a = 0.15$ (corresponding to a wave height $A = 2a = 0.3$). The initial condition is a numerically exact Stokes wave generated by Fenton's method [21]. The numerical parameters are $M = 4,\ \Delta t = 0.01$ and $N_1 \times N_2 = 64 \times 16$ grid points for a domain of size $[0, 2\pi] \times [0, 1.6]$. Since the solution is invariant in the transverse direction (x_2-direction), we do not need to specify a large domain width. We have made sure that the time step is much smaller

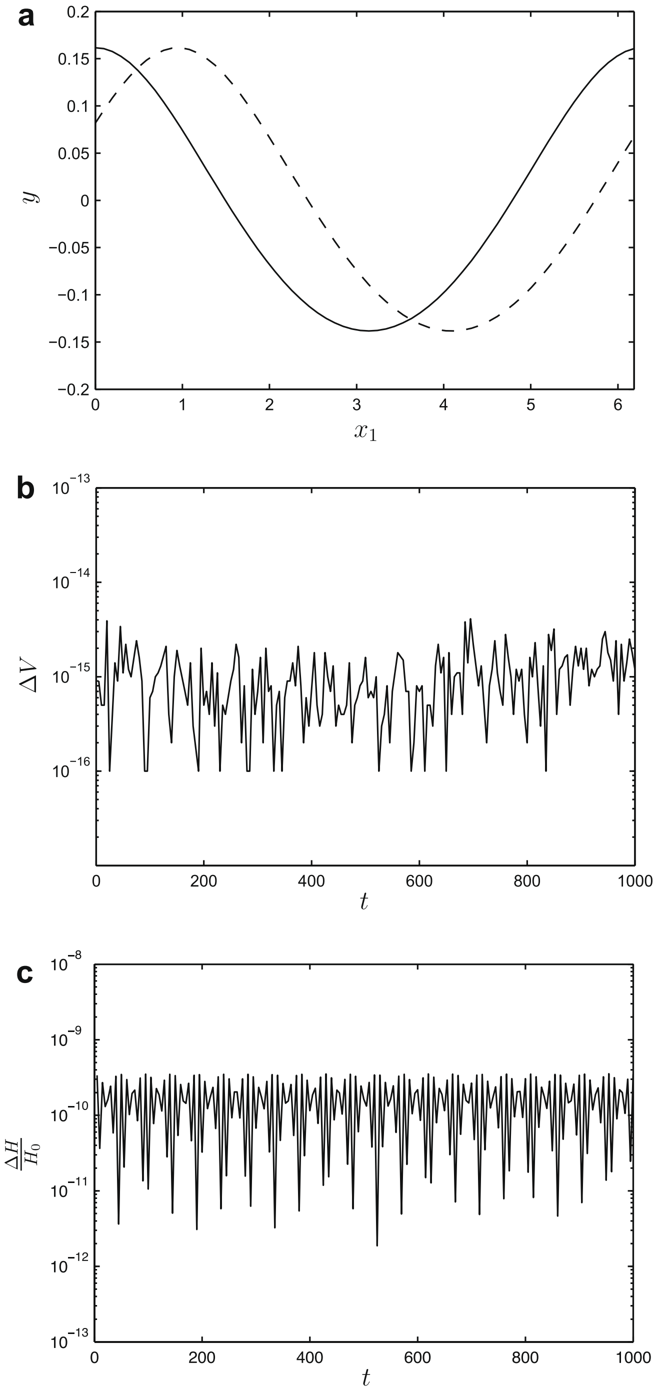

Fig. 3. Evolution of a Stokes wave of amplitude $a = 0.15$ and wavenumber $k_1 = 1$: (a) cross-sectional wave profiles at $t = 0$ (solid line) and $t = 1000$ (dashed line), (b) absolute error on mass vs. time, and (c) relative error on energy vs. time.

than the wave period $T = 2\pi/\omega$ and the integration time spans about a hundred wave periods. Fig. 3(a) shows the wave profiles at $t = 0$ and $t = 1000$, in the central cross-section $x_2 = 0.8$. We see that the initial wave shape is preserved very well over time. No filtering was used at any time during this simulation. The evolution of the total mass (10) and total energy (9) associated with this Stokes wave is depicted in Fig. 3(b) and (c). Both quantities are conserved very well throughout the computation, with an absolute error of $O(10^{-15})$ (near machine precision) and a relative error of $O(10^{-8}\%)$ for V and H respectively. These errors are calculated relative to the initial values V_0 and H_0 at time $t = 0$. Here, for V, we evaluate the absolute error (and not the relative error) because V_0 is near machine precision for a Stokes wave.

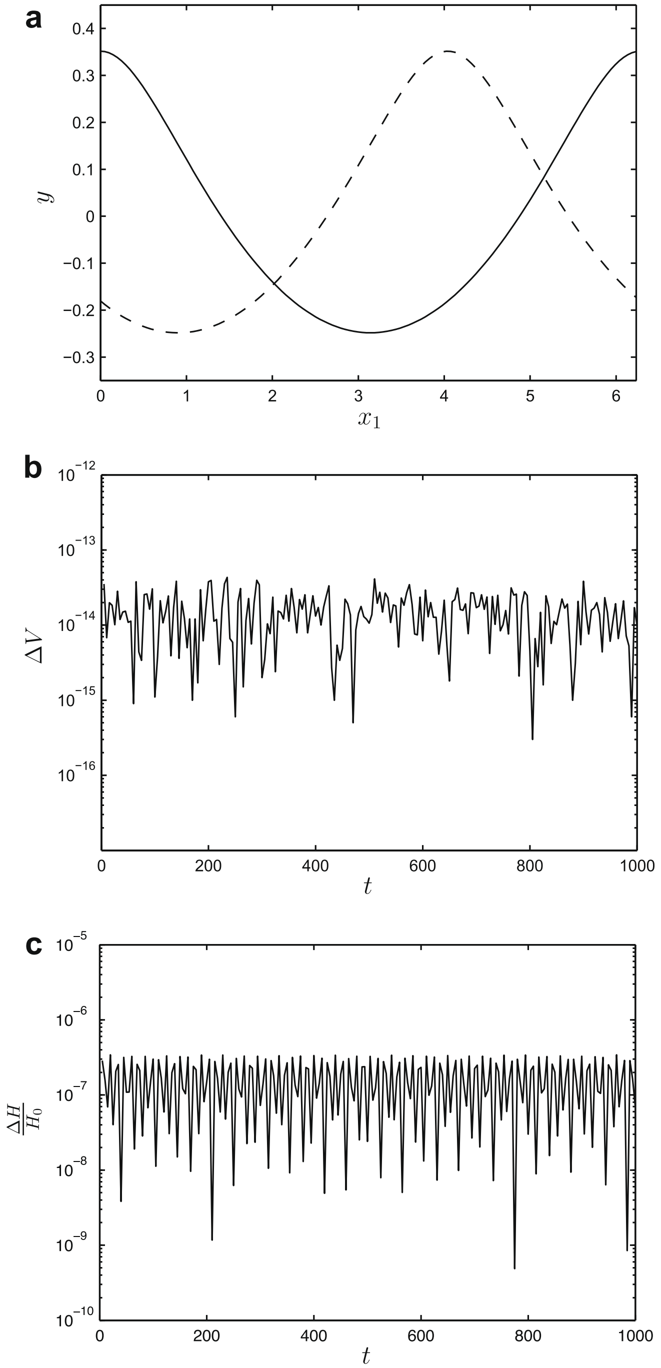

Fig. 4. Evolution of a Stokes wave of amplitude $a = 0.3$ and wavenumber $k_1 = 1$: (a) cross-sectional wave profiles at $t = 0$ (solid line) and $t = 1000$ (dashed line), (b) absolute error on mass vs. time, and (c) relative error on energy vs. time.

For larger-amplitude Stokes waves, we have found it necessary to use filtering (Hou and Li's filter (29)) to run simulations over a sufficiently long time. This is the case e.g. for $a = 0.3(k_1 = 1)$ which is illustrated in Fig. 4. All wave characteristics (profile, mass and energy) are preserved very well up to $t = 1000$. In particular, Hou and Li's filter does not seem to induce any trend in the conservation of V and H (such as a decrease in mass and energy). This supports the fact that this filtering technique is effective at suppressing high-wavenumber numerical instabilities, while keeping the solution's spectrum essentially unaffected.

We point out again that these tests are long-time simulations as compared to the wave period. For the two Stokes waves considered ($a = 0.15, 0.3$), the wave speed and period are $(c, T) = (1.01, 6.21)$ and $(1.05, 6.00)$, respectively (which are close

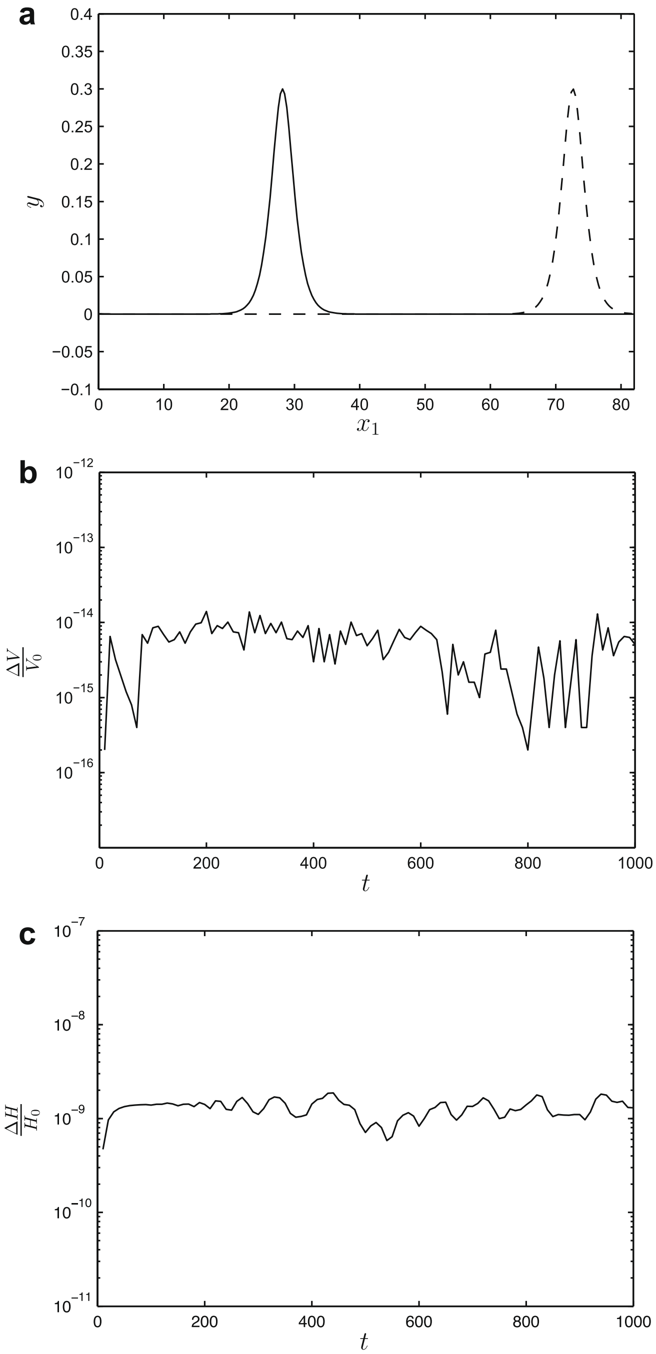

Fig. 5. Evolution of a solitary wave of height $a = 0.3$: (a) cross-sectional wave profiles at $t = 0$ (solid line) and $t = 1000$ (dashed line), (b) relative error on mass vs. time, and (c) relative error on energy vs. time.

to the linear values $c = 1,\ T = 2\pi$ for $k_1 = 1$). Therefore, over the time interval [0,1000], these waves have propagated about a hundred times through the periodic domain $[0, 2\pi]$. It is because of the periodic boundary conditions that the initial and final solutions are located close to each other in Figs. 3 and 4(a).

4.2.2. Progressive solitary waves

We next consider the propagation of a progressive solitary wave of amplitude $a = A = 0.3$ in shallow water ($h = 1$). The initial condition is a numerically exact solitary wave generated by Tanaka's method [58,13]. The numerical parameters are $M = 4,\ \Delta t = 0.01$ and $N_1 \times N_2 = 256 \times 16$ grid points over the domain $[0, 82] \times [0, 1.6]$. Similarly to the previous situation, the initial (two-dimensional) wave shape is preserved very well up to $t = 1000$, as shown in Fig. 5(a). Mass and energy are also conserved very well, with relative errors of $O(10^{-12}\%)$ and $O(10^{-7}\%)$ respectively (Fig. 5b and c). Again, no filtering was required to stabilize the numerical solution. The simulation time can be viewed here as long compared to the linear wave period $T = 2\pi$ (in shallow water with $h = 1$). For $a = 0.3$, the solitary wave speed is $c = 1.14$. Therefore, over the time interval [0,1000], this wave has propagated a dozen times through the periodic domain [0,82].

We have also checked the reversibility of the solution, which is associated with the time reversal symmetry $(t, \eta, \xi) \mapsto (-t, \eta, -\xi)$ of the equations of motion (6) and (7) [12]. Fig. 6 depicts the same solitary wave as in Fig. 5(a), along with the solution obtained by running the code backward in time (wave profile in crosses) starting from the final result at $t = 1000$. The excellent match between this solution and the initial one at $t = 0$ is strong evidence of the ability of the symplectic scheme to preserve the reversibility of the equations, even for a long integration time. More quantitatively, the L^2 difference between these two solutions is found to be 4.22×10^{-9}. This confirms the effectiveness of the fixed-point iterative procedure for solving (26) and (27), which only produces very small errors.

To further test our model in this situation, we have run a simulation for a larger amplitude $a = 0.6$, which is illustrated in Fig. 7. Such a solution corresponds to a highly nonlinear solitary wave and, accordingly, we have used $M = 6$ and applied filtering (ideal filter (28) with $v = 0.9$) to ensure that the simulation is stable up to $t = 1000$. We can see again in this example that, by only using a small amount of filtering, the numerical results are quite satisfactory in terms of conservation of wave profile, mass and energy, even with a high level of nonlinearity. Here, the relative errors on V and H are $O(10^{-12}\%)$ and $O(10^{-4}\%)$ respectively, and no significant decreasing or increasing trend is observed.

4.2.3. Modulational instability

Our third test case concerns the Benjamin–Feir (or modulational) instability of a deep-water Stokes wave. It is well-known that Stokes waves are unstable to sideband perturbations, in which case sideband frequencies gain energy at the expense of the carrier wave through four-wave interactions. Unlike linear instabilities, this weakly nonlinear instability does not go unbounded, which results in a cyclic, recurrent exchange of energy between the carrier wave and sideband frequencies.

Following Dommermuth and Yue [20], we specify as initial condition a Stokes wave of steepness $k_1 a = 0.13$ and wavenumber $k_1 = 9$, modulated by two Airy sideband waves:

$$\begin{aligned} \eta(x,0) &= \eta_0 + \varepsilon a\left[\cos\left(k_l x_1 - \frac{\pi}{4}\right) + \cos\left(k_r x_1 - \frac{\pi}{4}\right)\right], \\ \xi(x,0) &= \xi_0 + \varepsilon a\left[\frac{1}{\sqrt{k_l}} e^{k_l \eta} \sin\left(k_l x_1 - \frac{\pi}{4}\right) + \frac{1}{\sqrt{k_r}} e^{k_r \eta} \sin\left(k_r x_1 - \frac{\pi}{4}\right)\right]. \end{aligned} \tag{33}$$

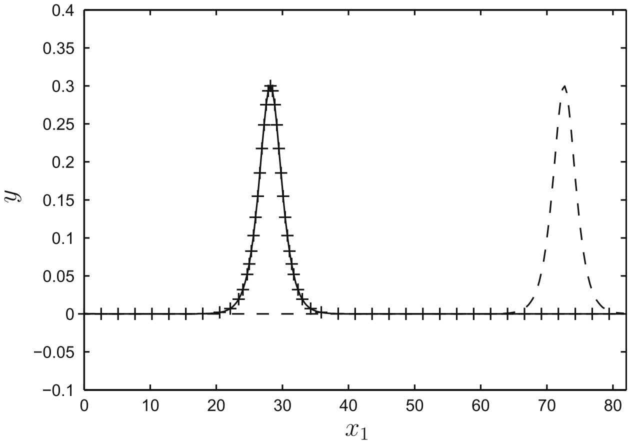

Fig. 6. Evolution of a solitary wave of height $a = 0.3$: cross-sectional wave profiles at $t = 0$ (solid line), $t = 1000$ forward in time (dashed line) and $t = 0$ backward in time (crosses). For clarity, not all the grid points are represented for the last solution.

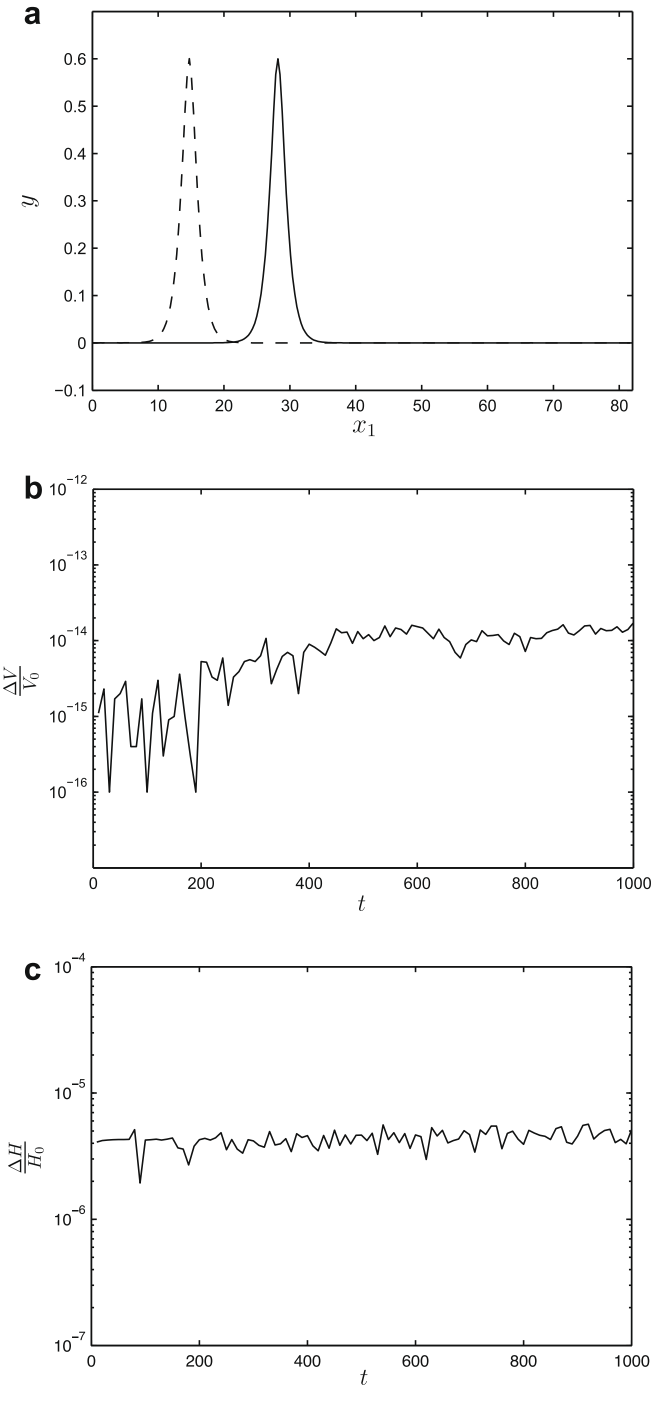

Fig. 7. Evolution of a solitary wave of height $a = 0.6$: (a) cross-sectional wave profiles at $t = 0$ (solid line) and $t = 1000$ (dashed line), (b) relative error on mass vs. time, and (c) relative error on energy vs. time.

Here $\eta_0,\ \xi_0$ stand for the Stokes wave solution, $\varepsilon = 0.1$ is the perturbation amplitude and $(k_l, k_r) = (7, 11)$ are the two side-band wavenumbers. This initial condition was used in [20] to compare with results of Stiassnie and Shemer [55] who solved the Zakharov equation numerically. We use $M = 4,\ \Delta t = 0.01$ (200 times smaller than the carrier wave period T) with no filtering, and the computational domain is $[0, 2\pi] \times [0, 2\pi]$ discretized with 64×64 grid points.

Fig. 8(a) plots the time histories of the fundamental ($k_1 = 9$), subharmonic ($k_1 = 7$) and superharmonic ($k_1 = 11$) modes until the computation breaks down at $t/T = 716$. Overall, our results compare significantly better than Dommermuth and

Yue's results do with those of Stiassnie and Shemer (see Fig. 3 in [20]). As in [55], we observe that the fundamental achieves a first minimum near $t/T = 60$ and its amplitude always remains higher than those of the sideband harmonics (except near the computation breakdown). These two evolve similarly even at their minima and maxima where their amplitudes remain relatively close together.

In addition, while Dommermuth and Yue's computation barely completed two cycles of recurrence before breaking down, ours was able to describe almost three full cycles. This computation breakdown is likely due to growth of high-wavenumber errors triggered by the Benjamin–Feir instability, leading eventually to wave breaking. The loss of recurrence which typically occurs after the first few cycles (possibly followed by computation breakdown), has also been experienced in other works using fully nonlinear numerical models, e.g. [42]. The gradual deterioration of energy conservation, as shown in Fig. 8(b), further indicates this trend to wave breaking. Energy is conserved to $O(10^{-3}\%)$ for $t/T \leqslant 600$ (past the maximum of the third cycle), after which there is a significant loss of accuracy, increasing the error to within 0.1% for the remaining duration of the simulation.

Note that using $M = 2$ would be sufficient to describe four-wave interactions, and we have checked that similar results are obtained in this case.

4.3. Crescent waves

We now examine the development of three-dimensional nonlinear water waves called crescent (or horseshoe) waves in deep water ($h = +\infty$). These waves arise as a result of three-dimensional wave interactions (class II instability of Stokes waves) and have been observed in a number of wavetank experiments [56,57]. Because of their physical relevance, and because of their nonlinear, unsteady and three-dimensional character, crescent waves have been extensively investigated in recent works, serving in particular as a test to assess the performance of three-dimensional nonlinear wave models [60,27,24,25].

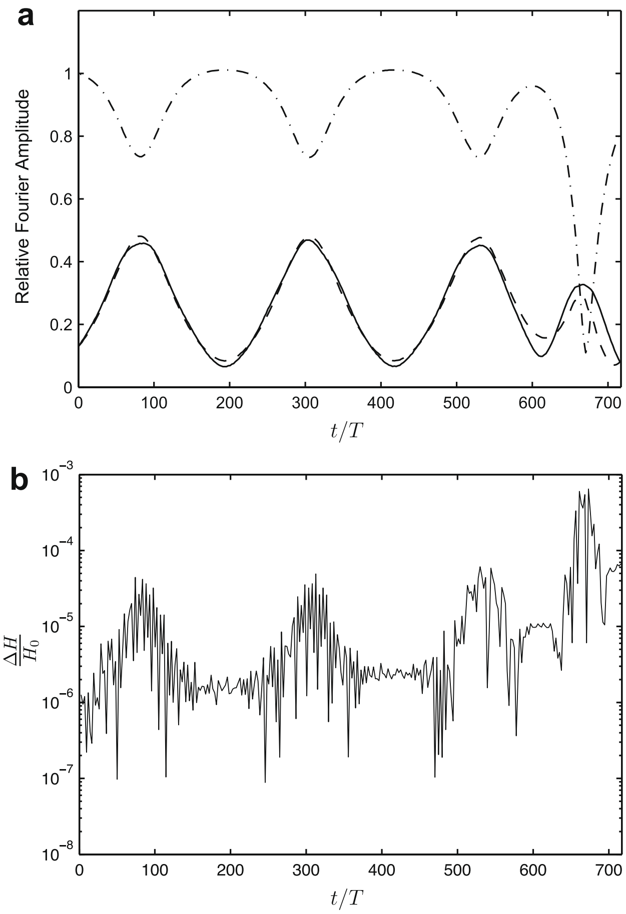

Fig. 8. Modulational instability of a Stokes wave of steepness $k_1a = 0.13$ and wavenumber $k_1 = 9$: (a) time histories of the fundamental ($k_1 = 9$, dashed-dotted line), subharmonic ($k_1 = 7$, dashed line) and superharmonic ($k_1 = 11$, solid line) modes relative to the initial amplitude of the fundamental, and (b) relative error on energy vs. time.

In order to reproduce such waves with the present model, we start the simulations with a deep-water Stokes wave (η_0, ξ_0) of steepness $k_1 a = 0.33$ and wavenumber $k_1 = 1$, to which small perturbations are added, of the form

$$\begin{aligned} \eta' &= \varepsilon a \sin(k_p x_1)\cos(k_q x_2), \\ \xi' &= \frac{-\varepsilon a}{\left(k_p^2 + k_q^2\right)^{1/4}} \cos(k_p x_1)\cos(k_q x_2) e^{(k_p^2+k_q^2)^{1/2}\eta_0} \end{aligned} \tag{34}$$

for the free surface and velocity potential respectively, as suggested in [60]. Here, the perturbation amplitude is $\varepsilon = 0.16$, and the wavenumbers are defined by $(k_p, k_q) = (k_1 + p, q)$, where p and q are the longitudinal and transverse perturbation wavenumbers. We use a rectangular domain given by $[0, L/p] \times [-L/q, L/q]$, where $L = 2\pi/k_1$, and discretized with 256×64 grid points. We set $M = 4$, $\Delta t = 0.01$, and $(k_p, k_q) = (1.5, 1.23)$ following [60]. Since the solution is highly unsteady and nonlinear, and rapidly steepens as it propagates, we used Hou and Li's filter [35] to prevent numerical instabilities. With these numerical parameters and this filter, energy is conserved to $O(0.01\%)$ in the computation.

Fig. 9 presents a sequence of free-surface profiles during the development of a crescent wave. At the initial time, the solution is only a slightly perturbed Stokes wave (Fig. 9a). However, as time progresses, it develops stronger longitudinal and transverse modulations leading to distinctive three-dimensional patterns. For example, at $t/T = 5.252$ when the crescent wave is well formed (T is the period of the unperturbed Stokes wave), we see that the front face of each pattern is steeper than the rear one. The forward fronts have sharper crests than the separating edges, forming semi-circular patterns facing forward (Fig. 9d). Our results are in good qualitative agreement with those obtained by Su [56], Xue et al. [60], Fuhrman et al. [27] and Fructus et al. [24]. In particular, the time duration required for the full development of a crescent wave $(t/T \sim 5)$ is consistent with that observed in numerical simulations of Xue et al. [60] and in wavetank experiments of Su

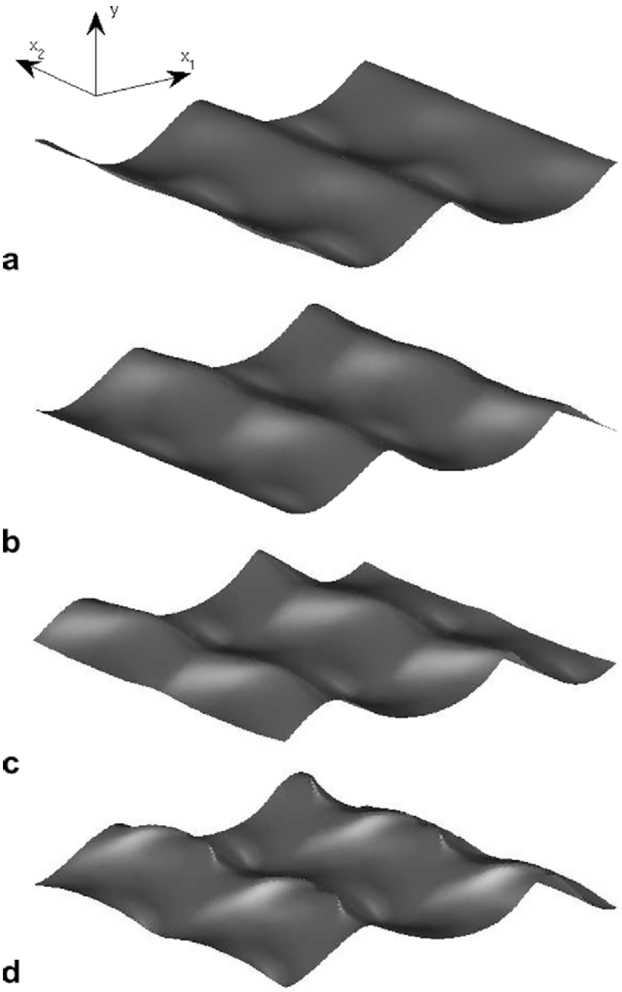

Fig. 9. Snapshots of the free surface showing crescent wave patterns at (a) $t/T = 0$, (b) $t/T = 1.592$, (c) $t/T = 3.183$, and (d) $t/T = 5.252$. The initial condition is a perturbed Stokes wave of steepness $k_1 a = 0.33$ and wavenumber $k_1 = 1$.

[56]. Shortly after $t/T = 5.252$, our computation eventually breaks down as the wave approaches breaking. Recall that, due to our formulation of the governing equations (the free surface being represented as the graph of a function $y = \eta(x, t)$), wave breaking is a phenomenon not permitted in the present algorithm.

In order to further demonstrate the accuracy of our model, we have performed a quantitative comparison with numerical results of Xue et al. [60] and Fructus et al. [24], and with experimental results of Su [56]. Fig. 10 shows the free-surface profiles in the vertical cross-sections $x_2 = -L/(2q)$ and $x_2 = -3L/(4q)$ at $t/T = 5.252$. Part (a) exhibits typical crescent features of alternating peaks and troughs, while part (b) depicts a regular (steepened) Stokes wave-like profile. Fig. 10(a) also defines the length and height parameters used by Su [56] to measure longitudinal characteristics of crescent waves. Ratios of these parameters are displayed in Table 1, comparing the values obtained from [56,60,24] and the present study. Overall, the agreement is good, which is remarkable given the fact that the initial disturbance specified in [56,24] most likely differs from that in the present simulation and in [60].

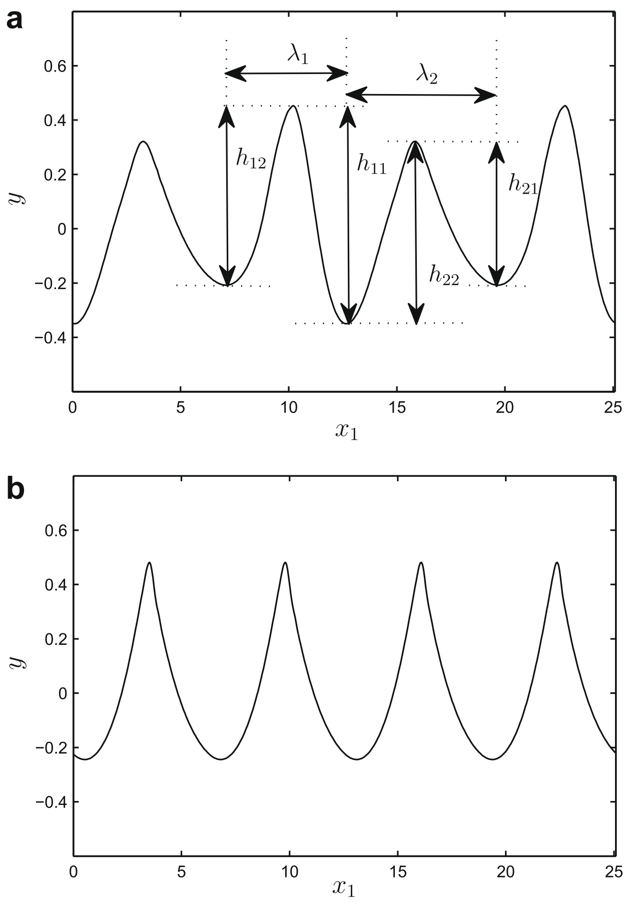

Fig. 10. Vertical cross-sections of a crescent wave pattern at (a) $x_2 = -L/(2q)$ and (b) $x_2 = -3L/(4q)$ at time $t/T = 5.252$. Characteristic length and height parameters according to Su [56] are also labeled in (a).

Table 1
Comparison of geometric parameters of crescent waves between the present simulation and other works. The parameters λ_1, λ_2, h_{11}, h_{12}, h_{21} and h_{22} are defined in Fig. 10; $S_{\max} = \max(|\partial_{x_1}\eta|)$ denotes the maximum slope.

Cases	λ_2/λ_1	h_{11}/h_{12}	h_{21}/h_{22}	h_{11}/h_{21}	$S_{\max}$
Su [56]	1.28	1.10	0.88	1.66	0.65
Fructus et al. [24] at $t/T = 16$	1.28	1.11	0.88	1.56	0.66
Xue et al. [60] at $t/T = 5.15$	1.17	1.26	0.75	1.60	0.51
Present model at $t/T = 5.17$	1.19	1.22	0.79	1.47	0.50

4.4. Rectangular and hexagonal waves

This section deals with another class of three-dimensional (short-crested) waves which typically arise from the oblique interaction of two traveling plane waves, or from the reflection of waves at non-normal incidence off vertical sea walls. Such waves are among the simplest three-dimensional waveforms, and have been observed in nature (especially in coastal regions) as well as in laboratory experiments. Because they constitute an essential building block in the theory of three-dimensional water waves, they have been a point of attention for many years. Studies range from theoretical [16,50,9] providing asymptotic solutions and existence results, experimental [34,33] to numerical [44,17,26,51] using both approximate and fully nonlinear models.

When nonlinearities are important, the character of these three-dimensional waves is known to depend strongly on water depth; more precisely on the aspect ratio of depth to wavelength. It has been observed that, in shallow water, two waves colliding at oblique incidence produce hexagonal patterns while, in deep water, the emerging pattern is rectangular waveforms. Previous computations of such waves have been performed either by looking for steady solutions of the Euler equations [17,51], or by solving approximate models [44,26]. Some early images of the rectangular/hexagonal wave dichotomy for short-crested waves in deep/shallow water can be found in [46,47]. A goal of this paper is to reproduce both hexagonal and rectangular wave patterns using the fully nonlinear time-dependent Euler equations.

We consider first the deep-water case. We specify as initial condition the first-order short-crested wave solution

$$\begin{aligned}
\eta(x,0) &= a\cos(k_1x_1)\cos(k_2x_2),\\
\xi(x,0) &= \frac{a\omega}{k}\frac{\cosh(k(\eta+h))}{\sinh(kh)}\sin(k_1x_1)\cos(k_2x_2)
\end{aligned} \tag{35}$$

following Hammack et al. [33] and Fuhrman and Madsen [26]. Here, $(k_1,k_2)=(k\sin\theta,k\cos\theta)$ so the initial wave profile is the superposition of two plane waves with identical amplitude $a/2$ and wavenumber k, moving in two different directions separated by an angle θ. We set $h=1,\ k=2\pi,\ a=0.024$ and $\theta=80.79^\circ$, which corresponds to a deep-water regime $(kh=2\pi)$ [26]. The numerical simulations are run for a domain of size $[0,2L_1]\times[0,L_2]$, where $L_1=2\pi/k_1$ and $L_2=2\pi/k_2$, discretized with 32×64 grid points. The temporal discretization is $\Delta t=0.01$ and the order of truncation of the DNO is $M=4$.

Fig. 11 shows a snapshot of the free surface at $t=1000$, which in fact does not differ much from the initial configuration. A top view of the wave patterns, comprising several wavelengths, and the corresponding contour plot are presented in Fig. 12. The gray color scale in Fig. 12(a) is adjusted so that the wave crests are brighter and the troughs are darker. In Fig. 12(b), the more rectangular contours correspond to the crests while the more rounded contours correspond to the troughs. These features agree well with those observed in experiments of Hammack et al. [33], and in numerical simulations of Craig and Nicholls [17], Fuhrman and Madsen [26] and Nicholls and Reitich [51]. In particular, the contour plot reveals nodal lines parallel to the x_1-direction, that separate the rectangular cells and have constant (near-zero) amplitude. Here, because the initial wave steepness is moderate, no filtering is required, the wave propagates with nearly constant form, and energy is conserved to $O(10^{-4}\%)$ throughout the computation.

We now turn our attention to hexagonal waves which typically form in shallow water. These three-dimensional waves are compatible with exact solutions of the Kadomtsev–Petviashvili equation and have been observed in wavetank experiments [34]. Recent computations of hexagonal waves have been performed by Milewski and Keller [44] in the framework of a long-wave model, and Craig and Nicholls [17] when looking for steady solutions of the Euler equations. Starting the simulations again with the initial condition (35), we set $h=1,\ k=0.52,\ a=0.16$ and $\theta=75.6^\circ$, which now corresponds to a shallow-water regime $(kh=0.52)$. The computational domain $[0,50]\times[0,48.33]$ is discretized with 128×128 grid points ($M=4$ and $\Delta t=0.01$).

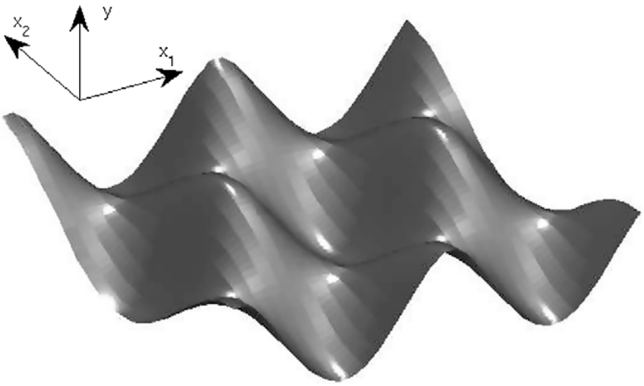

Fig. 11. Snapshot of the free surface at $t=1000$ showing rectangular wave patterns in deep water $(kh=2\pi)$.

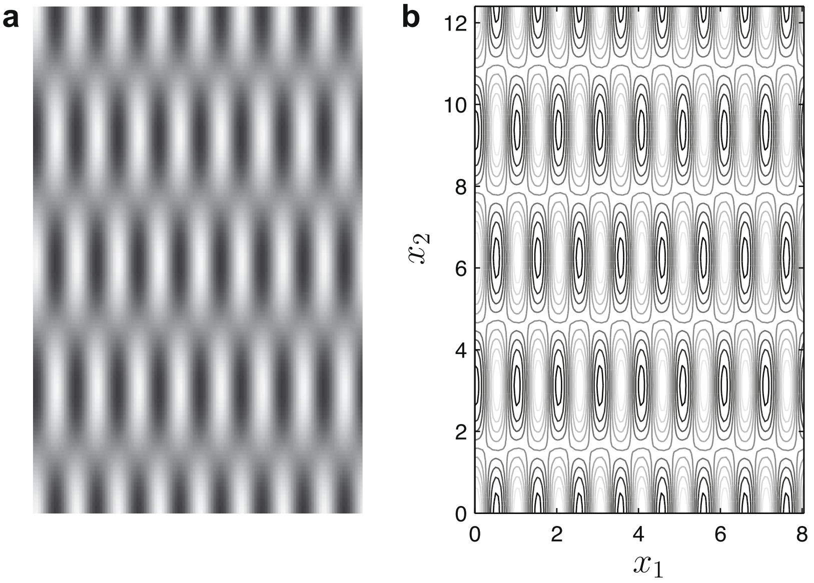

Fig. 12. Bright–dark top view (a) and contour plot (b) of rectangular wave patterns in deep water ($kh = 2\pi$) at $t = 1000$.

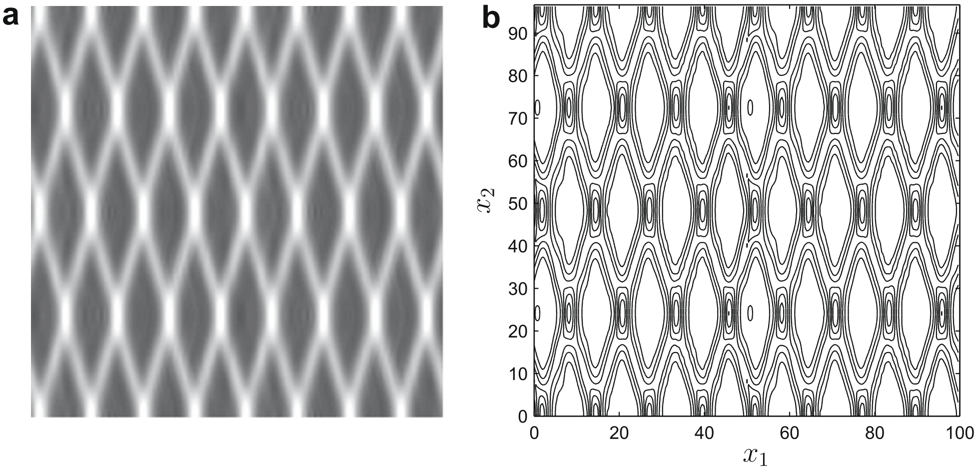

Fig. 13. Bright–dark top view (a) and contour plot (b) of hexagonal wave patterns in shallow water ($kh = 0.52$) at $t = 138$.

The bright–dark top view and contour plot in Fig. 13 clearly show hexagonal wave patterns separated by nodal lines having a zigzag structure. These zigzag nodal lines correspond to the wave crests. We see in Fig. 14 that these wave patterns have very flat troughs and steep crests, which contrasts with the smoother features of rectangular wave patterns (Fig. 11). Our results compare qualitatively well with wavetank experiments of Hammack et al. [34], and with numerical simulations of Milewski and Keller [44] and Craig and Nicholls [17]. Here, we needed to use filtering (Hou and Li's filter (29)) to prevent numerical instabilities which are likely promoted by the nonlinear development of the solution (flat troughs and steep crests). We also point out that the present simulation of hexagonal waves is highly unsteady. The solution evolves from the initial condition (35) to hexagonal wave patterns, and once these are formed, they are not stable. These patterns destabilize and then reform, and this cycle seems to repeat itself in time. This may be explained by the use of the first-order solution (35) for the initial condition, as suggested by Fuhrman and Madsen [26], which results in a release of spurious free first harmonics due to neglected steady third-order contributions. It would be of interest in the future to investigate the stability of hexagonal waves in further detail [37,40]. To our knowledge, this is still an open problem.

To further reveal the differences between rectangular and hexagonal waves, we plot in Fig. 15 vertical cross-sections of the free-surface profiles in the x_1-direction for the two previously described solutions ($a = 0.024$ in deep water and $a = 0.16$ in shallow water). These cross-sections are chosen at two different x_2-positions ($x_2 = L_2/4$ and $x_2 = L_2/2$). The cross-section

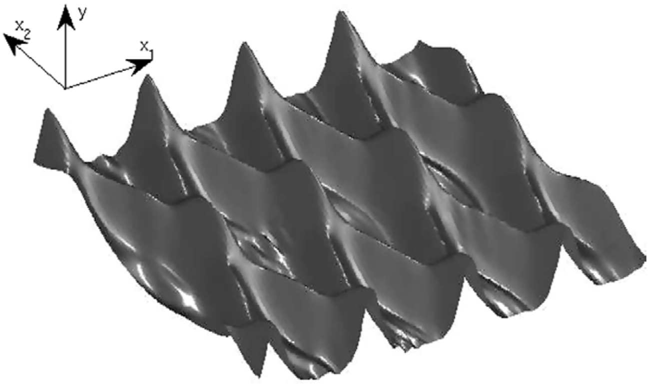

Fig. 14. Snapshot of the free surface at $t = 138$ showing hexagonal wave patterns in shallow water ($kh = 0.52$).

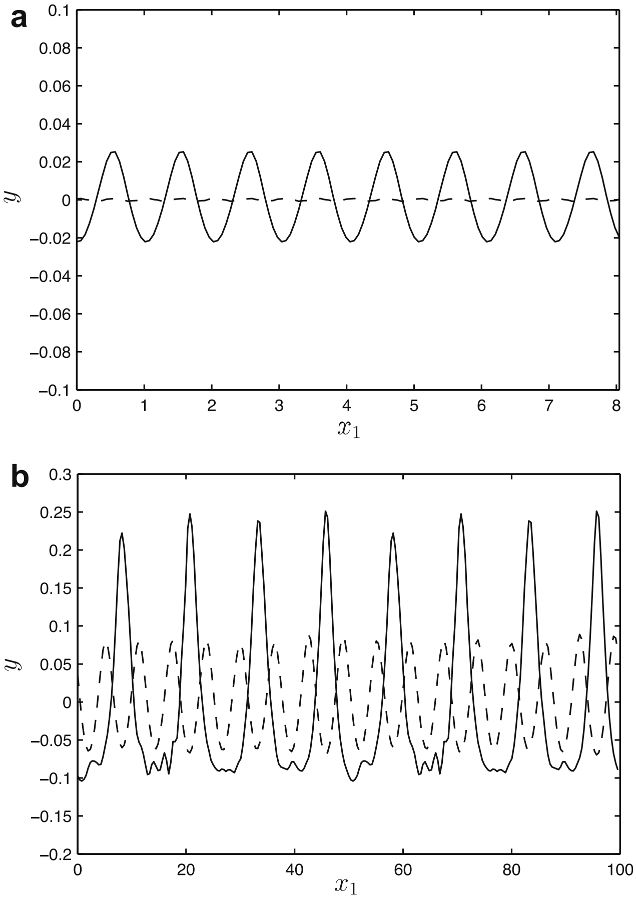

Fig. 15. Vertical cross-sections of (a) a rectangular wave pattern ($a = 0.024$) at $t = 1000$ and (b) a hexagonal wave pattern ($a = 0.16$) at $t = 138$. The dashed lines correspond to vertical cross-sections at $x_2 = L_2/4$, while the solid lines correspond to vertical cross-sections at $x_2 = L_2/2$.

$x_2 = L_2/4$ (dashed line) goes along a nodal straight line for $a = 0.024$ (Fig. 15(a)), and along a zigzag structure for $a = 0.16$ (Fig. 15(b)), as indicated in Fig. 5 in [33]. The near-zero amplitude of the dashed profile in Fig. 15(a) is typical of the nodal lines separating rectangular cells for solutions in deep water. The cross-section $x_2 = L_2/2$ (solid line) cuts through the middle of rectangular cells for $a = 0.024$, and through the middle of hexagonal cells for $a = 0.16$. The solid profile in Fig. 15(b) clearly indicates steeper and larger-amplitude crests as well as flatter troughs for solutions in shallow water. These features are similar to those observed in the traveling wave solutions derived by Chen and Iooss [9] for a three-dimensional Boussinesq system (see Figs. 1 and 2 in [9]).

5. Conclusions

We have developed a numerical model for fully nonlinear, three-dimensional surface water waves on infinite or finite depth. Similarly to the three-dimensional model of Bateman et al. [3] and, as an extension of the work of Craig and Sulem [19], it is based on Zakharov's Hamiltonian formulation in which the problem is reduced to a lower-dimensional computation involving surface variables alone. This is achieved by introducing the DNO which is expressed in terms of a convergent Taylor series expansion in powers of the surface elevation. Each term in this Taylor series is obtained from a recursion formula and is efficiently computed by a pseudospectral method using the fast Fourier transform.

We have developed a symplectic, implicit, fourth-order Runge–Kutta scheme for the time integration of the Hamiltonian equations of motion. The choice of an implicit scheme is motivated by the fact that the canonical variables η and ξ are coupled in a complicated nonlinear way through the DNO, which implies that a large nonlinear system must be solved at each time step. Nevertheless, this time integrator allows for an exact evaluation of the linear terms when combined with the pseudospectral method for space discretization, and the resulting nonlinear system can be solved at reasonable cost by fixed-point iteration. Our results show that this symplectic scheme has excellent conservative and reversible properties over long times of integration, and only a few iterations are needed to solve the nonlinear system in all of our applications. Note that, in some cases (modulational instability and crescent waves), we have observed that energy conservation quickly deteriorates after some period of time, followed by the computation breakdown (as also reported by other authors using different numerical models). We believe this is most likely due to the nonlinear character of these specific situations which either promotes the growth of high-wavenumber errors or leads to the physical wave breaking.

We have performed detailed numerical tests on the convergence of the Taylor series for the DNO, with respect to various numerical and physical parameters, including de-aliasing. Our tests confirm the exponential convergence with the order of truncation M. However, for relatively large wave amplitudes, there is an optimal value of M above which convergence quickly deteriorates; this phenomenon being related to the ill-conditioning of the expansion method for the DNO. The finer the spatial resolution, or the more aliased the computation, the smaller this optimal value.

We have also performed tests to assess the accuracy of the time integration method by simulating the long-time evolution of two types of steadily progressing waves, Stokes waves in deep water and solitary waves in shallow water. Overall, wave characteristics such as mass, energy and surface profiles are all very well-conserved. However, we have found it necessary to use filtering to simulate accurately the development of large-amplitude or highly deformed waves. In these cases, filtering is needed to suppress spurious high-wavenumber instabilities. For this purpose, we have tested two types of filter, an exponential and ideal filter, which are found to perform very well in our long-time simulations.

Finally, we have applied our numerical model to the simulation of three-dimensional nonlinear waves both in deep and shallow water. These include crescent, rectangular and hexagonal wave patterns. Our computations agree well with other existing experimental and numerical results.

Possible extensions of the present model include three-dimensional surface waves over a variable bottom topography, for which a modification of this method is suitable [15,32], and the development of an optimized/parallelized code [46] in order to make large-scale problems (with a large number of grid points) more tractable. These directions of inquiry are envisioned for future work.

Acknowledgments

The authors thank W. Craig, D.P. Nicholls and C. Sulem for encouragement and helpful discussions. Support from the University of Delaware Research Foundation and the National Science Foundation through Grant No. DMS-0625931 is gratefully acknowledged.

References

[1] W. Artiles, A. Nachbin, Nonlinear evolution of surface gravity waves over highly variable depth, Phys. Rev. Lett. 93 (2004) 234501.
[2] G.R. Baker, D.I. Meiron, S.A. Orszag, Generalized vortex methods for free-surface flow problems, J. Fluid Mech. 123 (1982) 477–501.
[3] W.J.D. Bateman, C. Swan, P.H. Taylor, On the efficient numerical simulation of directionally spread surface water waves, J. Comput. Phys. 174 (2001) 277–305.
[4] J.T. Beale, A convergent boundary integral method for three-dimensional water waves, Math. Comput. 70 (2001) 977–1029.
[5] J.L. Bona, M. Chen, J.-C. Saut, Boussinesq equations and other systems for small-amplitude long waves in nonlinear dispersive media. II. The nonlinear theory, Nonlinearity 17 (2004) 925–952.
[6] J.L. Bona, T. Colin, D. Lannes, Long wave approximations for water waves, Arch. Ration. Mech. Anal. 178 (2005) 373–410.
[7] A. de Bouard, W. Craig, O. Días-Espinosa, P. Guyenne, C. Sulem, Long wave expansions for water waves over random topography, Nonlinearity 21 (2008) 2143–2178.
[8] J.P. Boyd, Chebyshev and Fourier Spectral Methods, Dover, New York, 2004.
[9] M. Chen, G. Iooss, Periodic wave patterns of two-dimensional Boussinesq systems, Eur. J. Mech. B/Fluids 25 (2006) 393–405.
[10] D. Clamond, J. Grue, A fast method for fully nonlinear water wave computations, J. Fluid Mech. 447 (2001) 337–355.
[11] R. Coifman, Y. Meyer, Nonlinear harmonic analysis and analytic dependence, Proc. Symp. Pure Math. 43 (1985) 71–78.
[12] W. Craig, On the Badulin, Kharif and Shrira model of resonant water waves, Physica D 152–153 (2001) 434–450.
[13] W. Craig, P. Guyenne, J. Hammack, D. Henderson, C. Sulem, Solitary water wave interactions, Phys. Fluids 18 (2006) 057106.
[14] W. Craig, P. Guyenne, H. Kalisch, Hamiltonian long wave expansions for free surfaces and interfaces, Commun. Pure Appl. Math 58 (2005) 1587–1641.
[15] W. Craig, P. Guyenne, D.P. Nicholls, C. Sulem, Hamiltonian long wave expansions for water waves over a rough bottom, Proc. Roy. Soc. Lond. Ser. A Math. Phys. Eng. Sci. 461 (2005) 839–873.

[16] W. Craig, D.P. Nicholls, Traveling two and three dimensional capillary gravity water waves, SIAM J. Math. Anal. 32 (2000) 323–359.
[17] W. Craig, D.P. Nicholls, Traveling gravity water waves in two and three dimensions, Eur. J. Mech. B. Fluids 21 (2002) 615–641.
[18] W. Craig, U. Schanz, C. Sulem, The modulation regime of three-dimensional water waves and the Davey–Stewartson system, Ann. Inst. Henri Poincaré Anal. Non Linéaire 14 (1997) 615–667.
[19] W. Craig, C. Sulem, Numerical simulation of gravity waves, J. Comput. Phys. 108 (1993) 73–83.
[20] D.G. Dommermuth, D.K.P. Yue, A high-order spectral method for the study of nonlinear gravity waves, J. Fluid Mech. 184 (1987) 267–288.
[21] J.D. Fenton, The numerical solution of steady water wave problems, Comput. Geosci. 14 (1988) 357–368.
[22] C. Fochesato, F. Dias, A fast method for nonlinear three-dimensional free-surface waves, Proc. Roy. Soc. Lond. Ser. A Math. Phys. Eng. Sci. 462 (2006) 2715–2735.
[23] M. Frigo, S.G. Johnson, The Fastest Fourier Transform in the West, Technical report MIT-LCS-TR-728, MIT, Cambridge, MA, 1997. <http://theory.lcs.mit.edu/fftw/>.
[24] D. Fructus, D. Clamond, J. Grue, Ø. Kristiansen, An efficient model for three-dimensional surface wave simulations. Part I: Free space problems, J. Comput. Phys. 205 (2005) 665–685.
[25] D. Fructus, C. Kharif, M. Francius, Ø. Kristiansen, D. Clamond, J. Grue, Dynamics of crescent water wave patterns, J. Fluid Mech. 537 (2005) 155–186.
[26] D.R. Fuhrman, P.A. Madsen, Short-crested waves in deep water: a numerical investigation of recent laboratory experiments, J. Fluid Mech. 559 (2006) 391–411.
[27] D.R. Fuhrman, P.A. Madsen, H.B. Bingham, A numerical study of crescent waves, J. Fluid Mech. 513 (2004) 309–341.
[28] R.S. Gibson, C. Swan, The evolution of large ocean waves: the role of local and rapid spectral changes, Proc. Roy. Soc. Lond. Ser. A Math. Phys. Eng. Sci. 463 (2007) 21–48.
[29] M.F. Gobbi, J.T. Kirby, G. Wei, A fully nonlinear Boussinesq model for surface waves. II. Extension to $O(kh^4)$, J. Fluid Mech. 405 (2000) 181–210.
[30] S.T. Grilli, P. Guyenne, F. Dias, A fully nonlinear model for three-dimensional overturning waves over an arbitrary bottom, Int. J. Numer. Meth. Fluids 35 (2001) 829–867.
[31] P. Guyenne, S.T. Grilli, Numerical study of three-dimensional overturning waves in shallow water, J. Fluid Mech. 547 (2006) 361–388.
[32] P. Guyenne, D.P. Nicholls, A high-order spectral method for nonlinear water waves over moving bottom topography, SIAM J. Sci. Comput. 30 (2007) 81–101.
[33] J.L. Hammack, D.M. Henderson, H. Segur, Progressive waves with persistent two-dimensional surface patterns in deep water, J. Fluid Mech. 532 (2005) 1–52.
[34] J. Hammack, N. Scheffner, H. Segur, Two-dimensional periodic waves in shallow water, J. Fluid Mech. 209 (1989) 567–589.
[35] T.Y. Hou, R. Li, Computing nearly singular solutions using pseudo-spectral methods, J. Comput. Phys. 226 (2007) 379–397.
[36] T.Y. Hou, P. Zhang, Convergence of a boundary integral method for 3-D water waves, Discrete Contin. Dyn. Syst. Ser. B 2 (2002) 1–34.
[37] M. Ioualalen, A.J. Roberts, C. Kharif, On the observability of finite-depth short-crested water waves, J. Fluid Mech. 322 (1996) 1–19.
[38] P.A.E.M. Janssen, Nonlinear four-wave interactions and freak waves, J. Phys. Oceanogr. 33 (2003) 863–884.
[39] T.B. Johannessen, C. Swan, On the nonlinear dynamics of wave groups produced by the focusing of surface-water waves, Proc. Roy. Soc. Lond. Ser. A Math. Phys. Eng. Sci. 459 (2003) 1021–1052.
[40] O. Kimmoun, M. Ioualalen, C. Kharif, Instabilities of steep short-crested surface waves in deep water, Phys. Fluids 11 (1999) 1679–1681.
[41] B. Leimkuhler, S. Reich, Simulating Hamiltonian Dynamics, Cambridge University Press, Cambridge, 2004.
[42] P.A. Madsen, H.B. Bingham, H. Liu, A new Boussinesq method for fully nonlinear waves from shallow to deep water, J. Fluid Mech. 462 (2002) 1–30.
[43] R.I. McLachlan, Symplectic integration of Hamiltonian wave equations, Numer. Math. 66 (1994) 465–492.
[44] P.A. Milewski, J.B. Keller, Three dimensional water waves, Stud. Appl. Math. 37 (1996) 149–166.
[45] A. Nachbin, A terrain-following Boussinesq system, SIAM J. Appl. Math. 63 (2003) 905–922.
[46] D.P. Nicholls, Traveling water waves: spectral continuation methods with parallel implementation, J. Comput. Phys. 143 (1998) 224–240.
[47] D.P. Nicholls, On hexagonal gravity water waves, Math. Comput. Simul. 55 (2001) 567–575.
[48] D.P. Nicholls, F. Reitich, A new approach to analyticity of Dirichlet–Neumann operators, Proc. Roy. Soc. Edinburgh Sect. A 131 (2001) 1411–1433.
[49] D.P. Nicholls, F. Reitich, Stability of high-order perturbative methods for the computation of Dirichlet–Neumann operators, J. Comput. Phys. 170 (2001) 276–298.
[50] D.P. Nicholls, F. Reitich, On analyticity of travelling water waves, Proc. Roy. Soc. Lond. Ser. A Math. Phys. Eng. Sci. 461 (2005) 1283–1309.
[51] D.P. Nicholls, F. Reitich, Stable, high-order computation of traveling water waves in three dimensions, Eur. J. Mech. B/Fluids 25 (2006) 406–424.
[52] M. Onorato, A.R. Osborne, M. Serio, Modulational instability in crossing sea states: a possible mechanism for the formation of freak waves, Phys. Rev. Lett. 96 (2006) 014503.
[53] U. Schanz, On the evolution of gravity – capillary waves in three dimensions, Ph.D. thesis, University of Toronto, 1997.
[54] H. Socquet-Juglard, K.B. Dysthe, K. Trulsen, H.E. Krogstad, Probability distributions of surface gravity waves during spectral changes, J. Fluid Mech. 542 (2005) 195–216.
[55] M. Stiassnie, L. Shemer, Energy computations for evolution of class I and class II instabilities of Stokes waves, J. Fluid Mech. 174 (1987) 299–312.
[56] M.-Y. Su, Three-dimensional deep-water waves. Part I. Experimental measurement of skew and symmetric wave patterns, J. Fluid Mech. 124 (1982) 73–108.
[57] M.-Y. Su, M. Bergin, P. Marler, R. Myrick, Experiments on nonlinear instabilities and evolution of steep gravity-wave trains, J. Fluid Mech. 124 (1982) 45–72.
[58] M. Tanaka, The stability of solitary waves, Phys. Fluids 29 (1986) 650–655.
[59] B.J. West, K.A. Brueckner, R.S. Janda, D.M. Milder, R.L. Milton, A new numerical method for surface hydrodynamics, J. Geophys. Res. 92 (1987) 11803–11824.
[60] M. Xue, H. Xü, Y. Liu, D.K.P. Yue, Computations of fully nonlinear three-dimensional wave–wave and wave–body interactions. I. Dynamics of steep three-dimensional waves, J. Fluid Mech. 438 (2001) 11–39.
[61] V.E. Zakharov, Stability of periodic waves of finite amplitude on the surface of a deep fluid, J. Appl. Mech. Tech. Phys. 9 (1968) 190–194.